

3GPP-Compliant Radar Cross Section Characterization of Indoor Factory Targets

Ali Waqar Azim*, Ahmad Bazzi*[†], Roberto Bomfin*, Marwa Chafii*[†]

*Engineering Division, New York University Abu Dhabi (NYUAD), UAE

[†]NYU WIRELESS, Tandon School of Engineering, New York University, Brooklyn, NY, USA

Emails: {ali.waqar.azim,ahmad.bazzi,roberto.bomfin,marwa.chafii}@nyu.edu

Abstract—The following paper presents a systematic 3rd Generation Partnership Project (3GPP)-compliant characterization of radar cross section (RCS) for indoor factory (InF) objects, including small and mid-sized unmanned aerial vehicles (UAVs), robotic arms, and automated guided vehicles (AGVs). Through measurements in the 25 GHz to 28 GHz range, we validate the 3GPP standardized log-normal distribution model for RCS for above-mentioned target objects. The 3GPP-complaint RCS parameters obtained for the small-sized UAV are in close agreement (< 1 dB deviation) with 3GPP agreed values. The mid-sized UAVs exhibit higher reflectivity compared to the small-sized UAV due to enhanced specular components attributed to material and lithium-ion battery packs. The robotic arm exhibits dynamic RCS behavior due to mechanical articulation, whereas UAVs show clear size-dependent reflectivity patterns in AGVs. Our findings provide empirical validation for RCS characterization for integrated sensing and communication channel modeling in InF environments.

Index Terms—Radar cross section, 3GPP standardization, UAVs, log-normal distribution, indoor factory.

I. INTRODUCTION

Integrated sensing and communication (ISAC) has emerged as one of the key vertical for upcoming 6G networks [1], promising to unify environmental perception and data transmission within shared infrastructure and spectral resources. ISAC channel modeling requires complete characterization of the propagation conditions and the objects present within the environment, where each object has a unique signature, which can be characterized by its radar cross section (RCS). The RCS is an important statistic for future ISAC designs, especially for multi-static target detection and power allocation [2].

The standardized 3rd Generation Partnership Project (3GPP) TR38.901 [3] channel model lacks ISAC-related components, including explicit RCS characterization of objects. Furthermore, it employs an oversimplified scattering paradigm that treats all objects as passive reflectors. Thus, these models fail to account for the target-specific RCS variations that are fundamental for sensing applications. To address this limitation, the 3GPP RAN1 working group has initiated the development of ISAC channel model, which will explicitly incorporate RCS-based target definitions within its framework. In the context of RCS characterization, a three parameter-based RCS modeling approach has been agreed upon, where the first parameter defines the mean RCS, the second captures angle-dependent contributions, and the third models RCS variations using a log-normal statistical distribution. In addition, the RAN1

working group has provided guidelines on how to model the three parameters for several objects, including small-sized and large-sized unmanned aerial vehicles (UAVs), humans, and automotive vehicles.

In 3GPP's RCS characterization approach, the degree of angular dependency varies across object classes. For instance, simplified models omitting angle dependence are employed for small-sized UAVs and humans, whereas RCS profiles requiring precise angle-dependent modeling are necessary for automotive vehicles and large-sized UAVs. However, other target objects commonly present in an indoor factory (InF) environment, such as mid-sized UAVs, robotic arms, and automated guided vehicles (AGVs), have not yet received explicit modeling guidance from the 3GPP. Although the agreed-upon three-parameter RCS model applies, the current standardization lacks specificity regarding the modeling of the angular component for these targets.

Recent advances in UAV sensing have yielded extensive work on RCS measurement and statistical modeling across various frequencies and platforms. [4] proposed a statistical recognition framework using RCS measurements at 15 and 25 GHz. Complementing this, [5] provided RCS measurements from 8.2 GHz to 18 GHz, while [6] evaluated machine learning and deep learning algorithms for RCS-based UAV classification. The survey by [7] outlines key radar classification and RCS modeling approaches for small UAVs. In the ISAC context, [8] reported monostatic and bistatic RCS measurements of UAVs, robotic arms, and AGVs at 25 GHz to 28 GHz. Moreover, [9] assessed RCS-based drone detection using 28 GHz measurements, and [10] analyzed RCS of UAVs across 26 GHz to 40 GHz. Existing literature still lacks RCS measurements for industrial assets such as robotic arms and AGVs. Researchers have yet to propose a standardized ISAC channel model that incorporates the three RCS parameters specified by 3GPP.

To provide a practical perspective, this paper presents a 3GPP-compliant RCS characterization methodology for InF targets, addressing three key challenges: (1) quantifying log-normal RCS fluctuations across target objects, (2) validating small-sized UAV parameters against 3GPP standards, and (3) establishing baseline RCS models for InF equipment.

The remainder of this paper is organized as follows: Section II details the 3GPP RCS standardization framework. Section III presents our RCS characterization methodology.

Section IV analyzes the experimental results, validating log-normal distribution fits 3GPP standard-based parameters and summarizes key findings regarding RCS characteristics of small/mid-sized UAVs, robotic arms, and AGVs. Finally, Section V draws conclusions.

II. STANDARDIZED RCS CHARACTERIZATION FRAMEWORK BY 3GPP

The 3GPP RAN#116bis agreement establishes that the standardized RCS characterization framework accounts for multiple deterministic and stochastic dependencies of the scattering properties of a physical object including object’s physical dimensions, material parameters, geometric configurations, orientation relative to the transceiver, the incident and scattered angles, and the operating frequency. Subsequent RAN#118bis agreement formalizes two models for RCS characterization. The first model implements RCS as multiplicative decomposition, i.e., $RCS = A \times B$ where A is the mean RCS value invariant to angle variations, and B captures stochastic fluctuations through a unit-mean log-normal distribution. The mean RCS term A serves as the primary parameter of object-specific properties and incorporates size/material/geometry effects and handles frequency scaling. The second model extends RCS modeling by explicitly incorporating an angular dependency term, resulting in $RCS = A \times B_1 \times B_2$, where B_1 is a deterministic angle-dependent function, and B_2 is generated by unit-mean log-normal distribution.

For UAVs with single scattering points in monostatic configurations, RAN#118bis specifically selects the three-component model, i.e., $RCS = A \times B_1 \times B_2$ with distinct implementations based on size class. Small-sized UAVs utilize $B_1 = 1$, i.e., 0 dB with A as the mean RCS value, while large-sized UAVs incorporate angle-dependent B_1 components while maintaining A as the mean RCS. In both cases, B_2 follows the standardized unit-mean log-normal distribution. Building upon these foundations, RAN#119bis specifies that for humans modeled as single scattering points in monostatic configurations, two RCS models are supported. The first model sets $B_1 = 0$ dB with A as mean RCS and B_2 following log-normal distribution, while the second model incorporates angle-dependent B_1 implemented either as: (i) antenna radiation pattern per TR38.901, (ii) analytic function, or (iii) lookup table, with B_2 maintaining the unit-mean log-normal characteristics. For vehicles with single scattering points, the framework mandates an explicit modeling for angle-dependent B_1 with the same implementation options, while multi-scatter point vehicle models prescribe five specific scattering locations (front, left, back, right, roof) each following the $RCS = A \times B_1 \times B_2$ formulation. The standard constrains B_2 through upper bounding $k\sigma$ dB where σ is the standard deviation of B_2 in dB, with $k = 3$ subsequently adopted in RAN#120bis.

The RAN#120bis agreements further refine bistatic and monostatic consistency requirements, mandating that bistatic RCS values must align with monostatic results when incident and scattered angles coincide. Moreover, the 3GPP RAN#120bis agreement has established standardized RCS

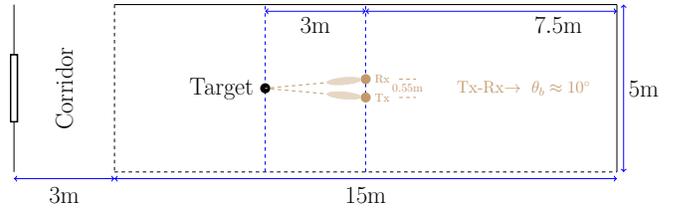


Fig. 1: The layout of the measurement environment.

parameters through its consensus-driven process, yielding definitive values for both small-sized UAVs and humans. For UAV characterization, the agreed parameters comprise $A = -12.81$ dBsm, $B_1 = 0$ dB, and $B_2 = 3.74$ dB. The identical three-parameter model extends to human targets with values $A = -1.37$ dBsm, $B_1 = 0$ dB, and $B_2 = 3.94$ dB. The standardized parameters originate from the 3GPP evaluation framework, which forms a standard format of the measurement data submitted by all participating members through systematic averaging.

III. RCS CHARACTERIZATION

A. RCS Characterization Methodology

In our RCS characterization approach, we follow the three-component model $RCS = A \times B_1 \times B_2$ with modeling the angle-dependent component, $B_1 = 0$ dB for mid-sized UAVs, robotic arms, and AGVs. The 3GPP standardization maintains uniformity in the treatment of A and B_2 across all object classes, including humans, UAVs, and vehicles, with the primary distinction arising only in B_1 . Although 3GPP explicitly defines angle-dependent B_1 for large-sized UAVs and vehicles, it does not provide guidance for mid-sized UAVs, robotic arms, and AGVs. Our RCS characterization methodology assumes $B_1 = 0$ dB as: (1) it aligns with the 3GPP’s treatment of target objects with negligible angle dependence (e.g. small-sized UAVs/humans), and (2) for our dynamic experimental conditions, angular effects are inherently embedded in the measurements as the UAV platforms undergo continuous flight rotations, while robotic arms and AGVs execute typical InF task-driven movements, ensuring angular diversity in the captured RCS statistics. Thus, the components A and B_2 describe the variations through the log-normal distribution, which provides a conservative and measurement-oriented baseline consistent with 3GPP’s framework.

B. Measurement Setup and Considerations

The measurement campaign was conducted in the KINESIS Lab, Core Technology Platforms, at NYU Abu Dhabi, a dedicated 5 m (width) \times 15 m (length) \times 8.5 m (height) indoor facility designed to emulate InF environments. The lab features characteristic InF architectural elements including elevated ceilings and open spatial configurations. The experimental layout is shown in Fig. 1.

The monostatic measurement testbed is shown in Fig. 2 which employs a collocated transmitter (Tx)/receiver (Rx). The measurement testbed parameters summarized in Table I. The Tx uses MATLAB-generated Zadoff-Chu (ZC) sequences of length 128 for waveform generation, upconverted to the

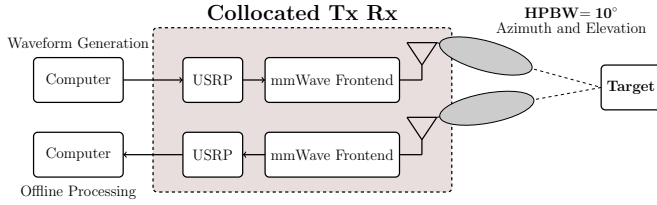


Fig. 2: Measurement testbed configuration.

TABLE I: Key System Parameters

Measurement Setup Parameters	
Operating Frequency	25 GHz to 28 GHz
Intermediate Frequency	3 GHz
RFIC	Sivers EVK02004
HPBW	10° (Azimuth and Elevation)
RFIC ADC	10 bits
USRP ADC	12 bits
Polarization	H-H
Measurement Conditions	LoS
USRP	B205mini
USRP Bandwidth	20 MHz
Signaling	Zadoff-Chu
Tx-Rx Height	1 m from ground
Dataset Size	300 MB
Location	NYU Abu Dhabi

25 GHz to 28 GHz via a Sivers EVK02004 RFIC interfaced with a B205mini USRP. The Rx chain performs downconversion and digitization using an identical USRP-RFIC pair. An intermediate frequency (IF) of 3 GHz is used at both the Tx and the Rx. During the measurements, the objects were positioned at the observation point located 3 m from the Tx-Rx baseline center, with both antennas boresighted (HPBW = 10° in elevation/azimuth) to ensure beam convergence at the observation point. Frequency calibration was performed in 1 GHz increments across the 25 GHz to 28 GHz band, with real-time processing to extract channel impulse responses (CIRs) from the received waveforms for offline processing. All the measurements were conducted in line-of-sight (LoS) propagation conditions with horizontal (H) polarization for both the Tx and the Rx.

C. Indoor Factory Targets and Measurement Conditions

Our measurements focus on objects prevalent in InF environments: (i) small-sized UAV, (ii) mid-sized UAV, (iii) robotic arm, and (iv) AGV, with detailed characteristics provided in Table II and visual representations in Figs. 3 and 4

For UAV measurements, both small and mid-sized platforms were in continuous rotational flight above the observation point, ensuring comprehensive angular coverage of backscatter reflections at the Rx. The vertical clearance between the ground and UAV underside for small-sized UAV was maintained 0.9 m and 0.6 m for the mid-sized UAV, while laser alignment fixed the geometric center at 1 m altitude for both platforms. The mid-sized UAV has dual lithium-ion batteries mounted laterally, whereas, for small-sized UAV has a top-mounted battery.

The second object is a robotic arm as shown in Fig. 4a. During the measurements, the robotic arm was placed at the observation point while it was executing tasks that are typical to InF operations. The seven joints in the robotic arm enabled



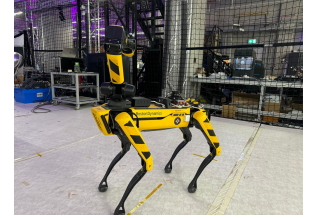
(a) Small-sized UAV

(b) Mid-sized UAV

Fig. 3: Small-sized and Mid-sized UAV test objects used in the study.



(a) Robotic Arm



(b) AGV

Fig. 4: Robotic arm and AGV test objects used in the study.

continuous motion through typical tasks, including pick-and-place operations, with a couple of them shown in Fig. 5. The robotic arm has a maximum height of 1640 mm, however, while emulating different tasks, the height was dynamically reduced during specific motions, resulting in variations in effective reflective surface area.

The third object is an AGV as shown in Fig. 4b. During the measurements, two different patterns were analyzed as shown in Fig. 6: (i) longitudinal motion toward/away from the observation point for front/back profiles and (ii) lateral motion along the observation point to capture side-profile RCS. Measurements included vertical traversal of a 20 cm non-conducting object at the observation point, simulating typical InF obstacle interaction scenarios while maintaining consistent orientation diversity.

D. Experimental Setup and RCS Evaluation Methodology

Our experimental setup employs a quasi-monostatic configuration. While ideal monostatic operation requires coincident Tx and Rx positions ($\theta = 0^\circ$), practical implementation necessitates spatial separation between the Tx and Rx antennas. The quasi-monostatic measurement configuration as shown in Fig. 7 employs a 55 cm Tx-Rx baseline separation $d_{Tx,Rx}$, producing an angular offset of $\theta \approx 10^\circ$ at the observation point. Both Tx-target $d_{Tx,tar}$ and Rx-target $d_{Rx,tar}$ distances are maintained at ≈ 3 m, with the antenna pair centrally positioned in the InF environment as shown in Fig. 1.

The measurements initiate with acquisition of reference CIR $h_{ref}(n)$ for all the operational frequencies, prior to target introduction. The reference measurements characterize the intrinsic contributions of environmental clutter and static scatterers within the measurement domain for the operating frequencies. $h_{ref}(n)$ serves as a baseline for subsequent target measurements, and allow to evaluate the reference power,

TABLE II: Specifications of the InF Objects Used in the Measurements.

Equipment	Dimensions	Mass	Materials
Small-Sized UAV (DJI Mavic 2 Pro)	Folded: $214 \times 91 \times 84$ mm Unfolded: $322 \times 242 \times 84$ mm	907g	Magnesium alloy, reinforced plastic, carbon fiber, glass, silicon components
Mid-Sized UAV (DJI Matrice 300 RTK)	Folded: $430 \times 420 \times 430$ mm Unfolded: $810 \times 670 \times 430$ mm	3.6-6.3kg	Carbon fiber-reinforced plastic, aluminum, plastic
Robotic Arm (KUKA LBR iiwa 14 R820)	Reach: 820 mm Height: 1640 mm (with arm)	≈ 30 kg	Aluminum, titanium, steel, plastic, polymer composites
AGV (Quadruped Robot) (Boston Dynamics Spot)	Length: 1100 mm; Width: 500 mm; Height: 610 mm (walking without arm)	≈ 32.7 kg	Aluminum, titanium, carbon fiber composites, polymer

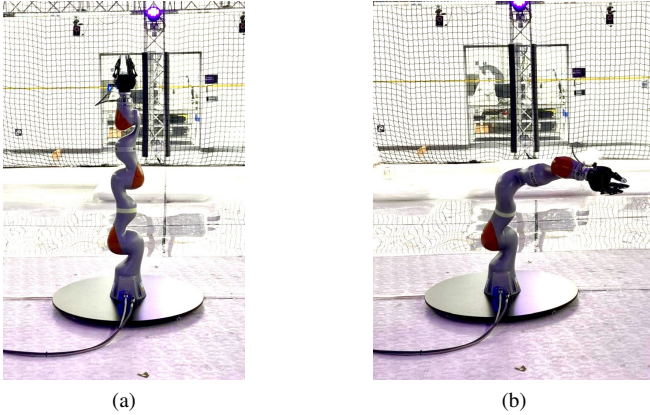


Fig. 5: Different motions of robotic arm during the measurements.



Fig. 6: The longitudinal and lateral motion of AGV during the measurements.

i.e., $P_{\text{ref}} = \sum_n |h_{\text{back}}(n)|^2$. P_{ref} quantifies the total energy of the background propagation environment by providing a scalar metric of the ambient clutter power level against which target reflections must be discriminated. Subsequently, the target-inclusive CIR, $h(n)$ is obtained for all the operating frequencies, capturing the composite effects of environmental scattering $h_{\text{ref}}(n)$ and target-specific reflections $h_{\text{tar}}(n)$. The total received power $P_{\text{tot}} = \sum_n |h(n)|^2$ decomposes into two primary components, that are, $P_{\text{tot}} = P_{\text{tar}} + P_{\text{ref}}$. Through differential power analysis, we isolate the target contribution as $P_{\text{tar}} = P_{\text{tot}} - P_{\text{ref}}$, effectively suppressing environmental clutter. Moreover, it is highlighted that the measurements were performed with high signal power, therefore, even a low variation in received power is above the clutter power and are detectable. P_{tar} computed for all the target object at all the operating frequencies. Since $d_{\text{Tx,tar}} = d_{\text{Rx,tar}} = d$, the target power P_{tar} directly relates to the RCS σ through the following radar equation:

$$P_{\text{tar}} = \frac{P_t G_t G_r \lambda^2 \sigma L}{(4\pi)^3 d^4} \quad (1)$$

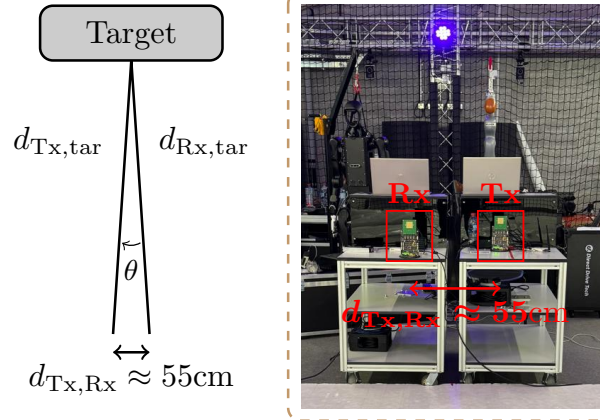


Fig. 7: Quasi-monostatic measurement setup.

where P_t is transmit power, G_t/G_r are antenna gains, λ is the wavelength, and L are unknown system losses.

The radar equation parameters excluding λ , d , and σ require precise calibration due to their system-specific nature. The calibration process determines a system factor $K(\lambda)$ through measurements where the Rx is positioned at the target location, i.e., observation point, where the procedure leverages the known free-space path loss relationship $P_r = \frac{P_t G_t G_r \lambda^2 L}{(4\pi)^2 d^2}$. Through these measurements, we compute the system factor as $K(\lambda) = P_r / (4\pi d^2)$, by normalizing the received power by $4\pi d^2$ (d is already known, i.e., 3 m), which ensures consistency between the single-path (calibration) and dual-path (RCS measurement) scenarios. The calibrated RCS is then derived as $\sigma = K^{-1}(\lambda) P_{\text{tar}}$. The approach ensures compensation for system-specific gains/losses through $K(\lambda)$. The calibration's validity rests on maintaining consistent system parameters (transmit power, antenna patterns, and receiver sensitivity) between calibration and measurement phases.

IV. RESULTS OF RCS FITTING TO LOG-NORMAL DISTRIBUTION

A. RCS Fitting to Log-normal Distribution

The measured RCS data is modeled using a log-normal distribution to capture its asymmetric and heavy-tailed characteristics from combined specular/diffuse reflections. The distribution parameters (μ , σ) are estimated via maximum likelihood, with goodness-of-fit (GoF) assessed through two complementary metrics. The first one is Kolmogorov–Smirnov (KS) statistic, i.e., $\text{KS} = \max |F(x) - F_{\mathcal{LN}}(x)|$ which quantifies the maximum deviation between empirical $F(x)$ and theoretical $F_{\mathcal{LN}}(x)$ cumulative distribution functions (CDFs),

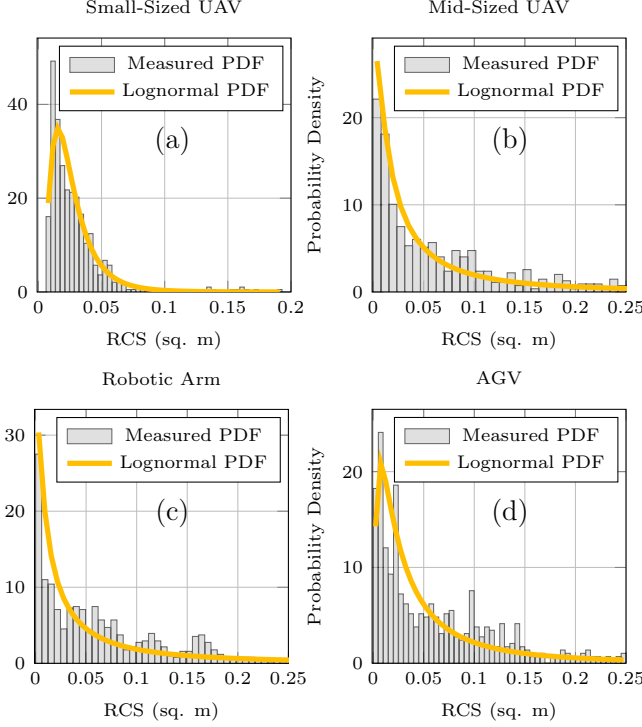


Fig. 8: Empirical and fitted lognormal PDFs for all the InF test objects at 28 GHz considered in the study.

TABLE III: Lognormal Distribution Parameters for Small-Sized UAV.

Freq. (GHz)	KS Stat ($\times 10^{-2}$)	MSE ($\times 10^{-3}$)	Parameters
25	8.8	2.3	$\mu = -3.9, \sigma = 1.4$
26	7.8	1.4	$\mu = -3.8, \sigma = 0.52$
27	8.7	2.7	$\mu = -3.83, \sigma = 1.74$
28	6	0.81	$\mu = -3.79, \sigma = 0.61$

and is sensitive to localized mismatches. The second one is the mean squared error (MSE), i.e., $MSE = \frac{1}{N} \sum_{i=1}^N (F(x_i) - F_{\mathcal{LN}}(x_i))^2$ which evaluates global fit quality across all N data points. Small KS/MSE values indicate a better fit.

Given space limitations, we present the fitting of RCS data to log-normal distribution by illustrating the probability density function (PDF) and CDF fit for all the objects at 28 GHz in Figs. 8 and 9. We can observe from Figs. 8 and 9 that log-normal distribution fits the measured RCS data reasonably well as also indicated by the GoF metrics provided in Tables III-VI. The behavior of the measured RCS data at other frequencies demonstrates consistent trends with variations primarily in parameter values rather than fundamental statistical behavior. The complete set of fitted log-normal parameters (μ, σ) for all the objects at different operating frequencies is provided in Tables III- VI.

TABLE IV: Lognormal Distribution Parameters for Mid-Sized UAV.

Freq. (GHz)	KS Stat ($\times 10^{-2}$)	MSE ($\times 10^{-3}$)	Parameters
25	10	2.3	$\mu = -3.5, \sigma = 1.42$
26	7.1	1.3	$\mu = -3.49, \sigma = 1.47$
27	14	6	$\mu = -3.47, \sigma = 1.96$
28	8.2	1.6	$\mu = -3.49, \sigma = 1.48$

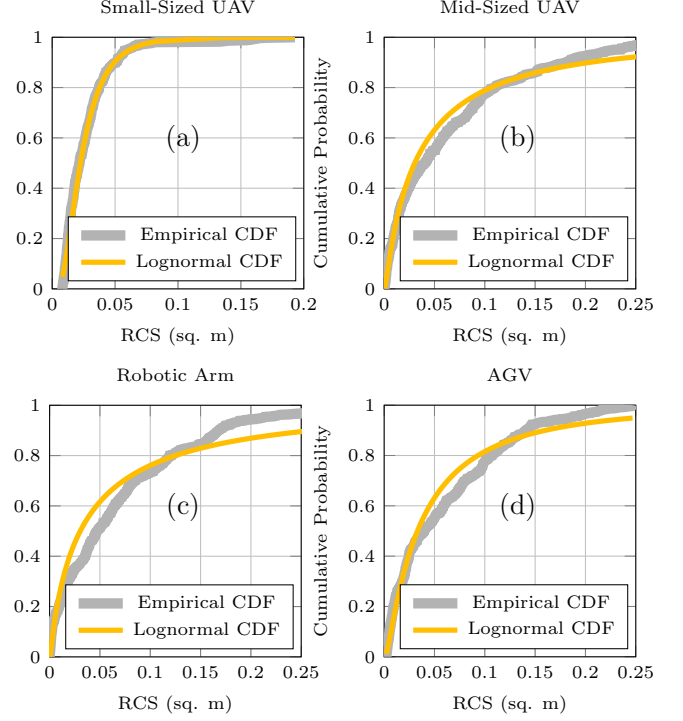


Fig. 9: Empirical and fitted lognormal CDFs for all the InF test objects at 28 GHz considered in the study.

TABLE V: Lognormal Distribution Parameters for Robotic Arm.

Freq. (GHz)	KS Stat ($\times 10^{-2}$)	MSE ($\times 10^{-3}$)	Parameters
25	11	3.2	$\mu = -3.43, \sigma = 1.79$
26	11	3.4	$\mu = -3.45, \sigma = 1.83$
27	8.5	2.6	$\mu = -3.48, \sigma = 1.82$
28	13	5	$\mu = -3.49, \sigma = 1.67$

B. A and B_2 Evaluation

The RCS follows a log-normal distribution characterized by parameters μ and σ , representing the mean and standard deviation of $\ln(X)$ where $X \sim \text{Lognormal}(\mu, \sigma^2)$. The mean RCS in linear scale is given by $\mathbb{E}[X] = e^{\mu + \sigma^2/2}$, with corresponding dBsm value $A = 10 \log_{10}(\mathbb{E}[X]) = 10 \log_{10}(e^{\mu + \sigma^2/2})$. The normalized variance B_2 in linear scale is derived as the squared coefficient of variation $B_2 = \text{Var}(X)/\mathbb{E}[X]^2 = e^{\sigma^2} - 1$, where the variance $\text{Var}(X) = (e^{\sigma^2} - 1)e^{2\mu + \sigma^2}$. When constrained to unit mean RCS ($\mathbb{E}[X] = 1$) as specified by 3GPP, this requires $\mu = -\sigma^2/2$, making B_2 dependent solely on σ^2 . The dB-scaled fluctuation parameter becomes $B_2(\text{dB}) = 10 \log_{10}(e^{\sigma^2} - 1)$, which properly represents relative RCS variations while being consistent with the log-normal framework.

TABLE VI: Lognormal Distribution Parameters for AGV.

Freq. (GHz)	KS Stat ($\times 10^{-2}$)	MSE ($\times 10^{-3}$)	Parameters
25	9.9	2.1	$\mu = -3.44, \sigma = 1.52$
26	9.9	2	$\mu = -3.44, \sigma = 1.10$
27	14	4.2	$\mu = -3.42, \sigma = 1.3$
28	8.8	2	$\mu = -3.4, \sigma = 1.22$

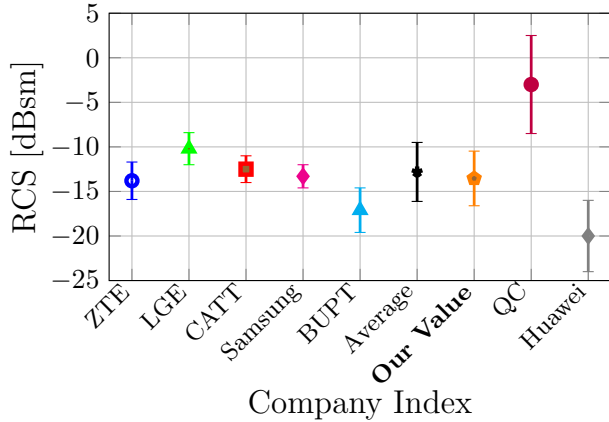


Fig. 10: Monostatic RCS for small-sized UAV (replicated from 3GPP).

C. Discussion

The parameters A and B_2 are computed for each object at every frequency point following the log-normal distribution analysis. The values are then averaged, with the final consolidated results presented in Table VII. The analysis of Table VII reveals distinct RCS characteristics across different UAV categories. As anticipated, mid-sized UAVs exhibit higher mean RCS values A compared to small-sized UAVs, with this difference attributable to three primary factors: (1) physical dimensions, (2) distinct material compositions, and (3) specular reflections from lithium-ion battery packs. The elevated B_2 values observed for mid-sized UAVs further support this interpretation, as rotational dynamics cause alternating strong specular returns when batteries face the radar and diffuse scattering when other surfaces are illuminated. The robotic arm demonstrates particularly interesting RCS behavior, with both high A and B_2 values. High A value is because of its predominantly metallic construction, while the significant B_2 emerges from measurement conditions capturing various operational movements. During movement sequences, the effective reflective area varies considerably during the articulation phases. The geometric variability produces the observed wide fluctuation in reflected signal strength, explaining both the high A and B_2 values. The reduced A value observed for the AGV results from two scattering mechanisms which result in higher number of diffused reflection: (1) the difference between the AGV's operational height (0.61 m) and the Tx-Rx antenna height (1 m), and (2) the longitudinal motion profile presents an effective reflective area that is much smaller than lateral reflective area.

The derived log-normal parameters for small-sized UAVs yield $A = -13.57$ dBsm and $B_2 = 3.065$ dB, demonstrating close agreement with 3GPP's standardized values of $A = -12.81$ dBsm and $B_2 = 3.74$ dB established through industry consensus. The marginal deviations ($\Delta A = 0.76$ dB, $\Delta B_2 = 0.675$ dB) fall well within the expected tolerance for RCS characterization, as evidenced from different industrial proposals. To further validate this agreement, we replicate the 3GPP's monostatic RCS distribution graph for small-sized UAVs, superimposing our values as shown in Fig. 10. The

TABLE VII: RCS values for the given targets considering 3GPP framework.

Target	A (dBsm)	B_1 (dB)	B_2 (dB)
Small-Sized UAV	-13.57	0	3.065
Mid-Sized UAV	-9.6	0	10.66
Robotic Arm	-8.165	0	13.54
AGV	-11.235	0	6.27

near-overlap of the curves particularly in the -15 dBsm to -10 dBsm range confirms accuracy of our RCS characterization approach with the 3GPP standardized values.

V. CONCLUSIONS

The experimental results provided in this paper establish three principal findings for InF RCS characterization: First, small-sized UAV measurements confirm 3GPP's standardized parameters within 1 dB tolerance, validating our evaluation methodology. Second, mid-sized targets exhibit 3 dB to 4 dB higher reflectivity than small UAVs, attributable to their larger physical dimensions and prominent battery reflections. Robotic arm demonstrate unique RCS signatures with 13.54 dB fluctuation variance during operation, directly correlated with mechanical articulation patterns. The AGV measurements further reveal how target object height and motion profiles affect scattering characteristics. Our findings validate our methodology for RCS characterization against the standardized 3GPP characterization approach.

REFERENCES

- [1] Haotian Liu, Zhiqing Wei, Jinghui Piao, Huici Wu, Xingwang Li, and Zhiyong Feng. "Carrier Aggregation Enabled MIMO-OFDM Integrated Sensing and Communication". *IEEE Transactions on Wireless Communications*, pages 1–1, 2025.
- [2] Zinat Behdad et al. "Multi-Static Target Detection and Power Allocation for Integrated Sensing and Communication in Cell-Free Massive MIMO". *IEEE Transactions on Wireless Communications*, 23(9):11580–11596, 2024.
- [3] 3rd Generation Partnership Project (3GPP). "Study on channel model for frequencies from 0.5 to 100 GHz". Technical Report TR 38.901, V16.1.0, 3GPP, 2020.
- [4] M. Ezuma, C. K. Anjinappa, M. Funderburk, and I. Guvenc. "Radar cross section based statistical recognition of UAVs at microwave frequencies". *IEEE Transactions on Aerospace and Electronic Systems*, 58(1):27–46, 2021.
- [5] M. Rosamilia, A. Balleri, A. De Maio, A. Aubry, and V. Carotenuto. "Radar detection performance prediction using measured UAVs RCS data". *IEEE Transactions on Aerospace and Electronic Systems*, 59(4):3550–3565, 2022.
- [6] M. Ezuma, C. K. Anjinappa, V. Semkin, and I. Guvenc. "Comparative analysis of radar-cross-section-based UAV recognition techniques". *IEEE Sensors Journal*, 22(18):17932–17949, 2022.
- [7] J. S. Patel, F. Fioranelli, and D. Anderson. "Review of radar classification and RCS characterisation techniques for small UAVs or drones". *IET Radar, Sonar & Navigation*, 12(9):911–919, 2018.
- [8] A. W. Azim, A. Bazzi, R. Bomfin, N. Giakoumidis, T. S. Rappaport, and M. Chafii. "Statistical and Deterministic RCS Characterization for ISAC Channel Modeling". *arXiv preprint arXiv:2502.11540*, 2025.
- [9] V. Semkin, M. Yin, Y. Hu, M. Mezzavilla, and S. Rangan. "Drone detection and classification based on radar cross section signatures". In *2020 International Symposium on Antennas and Propagation (ISAP)*, pages 223–224. IEEE, 2021.
- [10] V. Semkin, J. Haarla, T. Pairen, C. Slezak, S. Rangan, V. Viikari, and C. Oestges. "Analyzing radar cross section signatures of diverse drone models at mmWave frequencies". *IEEE Access*, 8:48958–48969, 2020.